A Eu^{3+}-Eu^{2+} ion redox shuttle imparts operational durability to Pb-I perovskite solar cells

Ligang Wang,[1] Huanping Zhou,[1]* Junnan Hu,[1] Bolong Huang,[2] Mingzi Sun,[2] Bowei Dong,[1] Guanghaojie Zheng,[1] Yuan Huang,[1] Yihua Chen,[1] Liang Li,[1] Ziqi Xu,[1] Nengxu Li,[1] Zheng Liu,[1] Qi Chen,[3] Ling-Dong Sun,[1]* Chun-Hua Yan[1]*

[1] Beijing National Laboratory for Molecular Sciences, State Key Laboratory of Rare Earth Materials Chemistry and Applications, PKU-HKU Joint Laboratory in Rare Earth Materials and Bioinorganic Chemistry, Key Laboratory for the Physics and Chemistry of Nanodevices, Beijing Key Laboratory for Theory and Technology of Advanced Battery Materials, Department of Materials Science and Engineering, College of Engineering, College of Chemistry and Molecular Engineering, Peking University, Beijing 100871, P.R. China

[2] Department of Applied Biology and Chemical Technology, The Hong Kong Polytechnic University, Hung Hom, Kowloon, Hong Kong SAR

[3] Department of Materials Science and Engineering, Beijing Institute of Technology, Beijing 100081, P. R. China

*Corresponding author. Email: happy_zhou@pku.edu.cn (H.Z.); yan@pku.edu.cn (C.H.Y.); sun@pku.edu.cn (L.D.S.)

Abstract:

The components with soft nature in the metal halide perovskite absorber usually generates Pb^0 and I^0 defects during device fabrication and operation. These defects serve as not only recombination centers to deteriorate device efficiency, but also degradation initiators to hamper device lifetimes. We show that the Eu^{3+}/Eu^{2+} ion pair acts as the "redox shuttle" that selectively oxidized Pb^0 and reduced I^0 defects simultaneously in a cyclical transition. The resultant device achieves a power conversion efficiency (PCE) of 21.52% (certified 20.52%) with substantially improved long-term durability. The device retained 92% and 89% of the peak PCE under 1 sun continuous illumination or heating at 85 Celsius for 1500 hours, and 91% of its original stable PCE after maximum power point tracking for 500 hours, respectively.

Keyword: perovskite, stability, photovoltaics, efficiency, optoelectronics

Device lifetime and power conversion efficiency (PCE) are the key factors determining the final cost of the electricity that solar cells generate. The certified PCE of perovskite solar cells has rapidly reached 23.3% over the past few years (*1-9*), which is on par with that of polycrystalline silicon and Cu(In,Ga)Se_2 solar cell. but poor device stability (*10-12*) under operating conditions prevents the perovskite photovoltaics from occupying even a tiny market share *(13, 14).* Generally, commercial solar cells give the warranty of 20 to 25 years lifetime with less than 10% drop of PCE, which corresponds to an average degradation rate of 0.5% per year (*15*). Compared to those inorganic photovoltaic materials, e.g. silicon (IV group) and CIGS (I-III-VI group) (*16*), the elements/components are mostly large and more polarized in organic-inorganic halide perovskite materials, such as I^-, MA^+, and Pb^{2+}. They construct soft crystal lattice prone to deform *(17),* which is vulnerable to various aging stresses such as oxygen, moisture (*18, 19*), and ultraviolet (UV) exposure *(20, 21).* By encapsulation (*22-24*), interface modification (13, *25-29*), and UV filtration, the device lifetime can be prolonged by the temporary exclusion of these external environmental factors.

Unfortunately, some aging stresses cannot be avoided during device operation, including light illumination, electric field, and thermal stress, upon which both I^- and Pb^{2+} in perovskites become chemically reactive to initiate the decomposition even they are well encapsulated (*30*). Because of the soft nature of I^-, Pb^{2+} ions, and Pb-I bonding, intrinsic degradation would occur in perovskite materials upon various excitation stresses, which finally induce PCE deterioration. On one hand, I^- is easily oxidized to I^0, which not only serve as carrier recombination centers, but also initiate chemical chain reactions to accelerate the degradation in perovskite layers (*31*). On the other hand,

Pb^{2+} is prone to be reduced to metallic Pb^0 upon heating or illumination, which has been observed in lead halide perovskite films (*32, 33*).

Pb^0 is a primary deep defect state that severely degrades the performance of perovskite optoelectronic devices (*34, 35*), as well as their long-term durability (*36*). Furthermore, most soft inorganic semiconductors with heavy elements are suffering similar instability, such as PbS (*37*), PbI_2 (*38, 39*), AgBr (*40*) etc. Several attempts have been reported to eliminate either Pb^0 or I^0 defects, like optimizing film processing (*41*), and additive engineering (*42-44*). To date, these additives are mostly sacrificial agents specific for one kind of defects, which diminish soon after they take effects. Long-term operational durability requires the simultaneous elimination of both Pb^0 and I^0 defects in perovskite materials in a sustainable manner.

We demonstrated constant elimination of Pb^0 and I^0 simultaneously in perovskite solar cells over their lifespan, which leads to remarkable stability improvement accompanying with the PCE promotion via introducing ion pair of $Eu^{3+}(f^6) \leftrightarrow Eu^{2+}(f^7)$ as the redox shuttle. In this cyclic redox transition, Pb^0 defects could be oxidized by Eu^{3+}, while I^0 defects could be reduced by Eu^{2+} at same time. Interestingly, Eu^{3+}/Eu^{2+} pair is not consumed during device operation, probably because of its nonvolatility and the suitable redox potential in this cyclic transition. Thus, the champion PCE of the corresponding device was promoted to 21.52% (certified, 20.52%) without current density-voltage (*J-V*) hysteresis. Devices with the Eu^{3+}/Eu^{2+} ion pair exhibited excellent shelf lifetime and thermal and light stability, which suggests that this approach may provide a universal solution to the inevitable degradation issue during device operation.

The reaction between Pb^0 and I^0 is thermodynamically favored and has a standard molar Gibbs formation energy for PbI_2(s) of −173.6 kJ/mol (*45*), which provides the driving force for eliminating both elementary defects. Unfortunately, simply mixing Pb and iodine powder only lead to limited formation of PbI_2, which suggests the presence of kinetic barriers at room temperature. To enable elimination of Pb^0 and I^0 defects in PSCs simultaneously across device lifespan, we propose the "redox shuttle" to oxidize Pb^0 and reduce I^0 independently, wherein they can be regenerated during the complete circle. It requires selectively oxidizing Pb^0 and reducing I^0 defects without introducing additional deep-level defects. After finely screening many possible redox shuttle additives, the rare earth ion pair of Eu^{3+}/Eu^{2+} was identified as the best candidate mostly owing to their appropriate redox potentials. Eu^{3+} could easily be reduced to Eu^{2+} with the stable half-full f^7 electron configuration to form the naturally associated ion pair. The redox shuttle can transfer electrons from Pb^0 to I^0 defects in a cyclical manner, wherein the Eu^{3+} oxidizes Pb^0 to Pb^{2+} and the formed Eu^{2+} simultaneously reduces I^0 to I^- (Fig. 1F). Thus, each ion in this pair is mutually replenished during defects elimination.

The proposed redox shuttle eliminates corresponding defects based on the following two chemical reactions:

$$2Eu^{3+} + Pb^0 \rightarrow 2Eu^{2+} + Pb^{2+} \quad (1)$$

$$Eu^{2+} + I^0 \rightarrow Eu^{3+} + I^- \quad (2)$$

We first explored the feasibility of Eu^{3+}/Eu^{2+} ion pair promote electron transfer from Pb^0 to I^0 in solution (Fig. 1A) by dispersing I_2 (25 mg) powder and metallic Pb powder (25 mg) in 2 mL of N,N-dimethylformamide (DMF) and isopropanol (IPA) that had a volume ratio of 1:10 as a

reference solution. The Eu^{3+}/Eu^{2+} ion pair was incorporated by further adding europium acetylacetonate ($Eu(acac)_3$) (11 mg) into the 2 mL solution. Under continuous stirring at 100 °C, the sample solution gradually turned from black to colorless with a large amount of yellow precipitates after 60 min, whereas the reference solution remained dark brown with little evidence of yellow precipitates.

Ultraviolet–visible (UV-Vis) spectra of the reference solution exhibited an absorption peak at ~370 nm (Fig. 1B), which we attributed to the presence of I^0 species (*36*) that was absent in the sample solution, which had an absorption peak at ~ 290 nm that we attributed to PbI_x species. Both I^0 and Pb^0 species were effectively converted to I^- and Pb^{2+} upon Eu^{3+} addition. X-ray diffraction (XRD) measurement on the precipitates revealed both PbI_2 (12.7 °, 25.9 °, 39.5 °) and metallic Pb (31.3 °, 36.2 °, 52.2 °) species in both cases (Fig. 1C). In the sample, the characteristic peak intensity ratio of PbI_2 to metallic Pb was greater larger than that of the reference (give numbers). This result further confirmed that Eu^{3+} could accelerate the conversion of Pb^0 and I^0 to Pb^{2+} and I^-, respectively.

When we added $Eu(acac)_3$ to the CH_3NH_3I solution of water/$CHCl_3$, we observed no I^0 species absorption peak in the corresponding UV–Vis spectrum (Fig. 1D), showing that Eu^{3+} selectively oxidizes Pb^0 rather than I^-. The stronger oxidizing agent of Fe^{3+} oxidize I^- species and the absorption peak of I^0 was present. We verified that Eu^{3+} was reduced to paramagnetic Eu^{2+} in $CH_3NH_3PbI_3$ ($MAPbI_3$) perovskite films with 1% (Eu/Pb, molar ratio) Eu^{3+} incorporated, which showed a strong signal in electron paramagnetic resonance (EPR) measurements (Fig. 1E) that was absent in Eu_2O_3 and in a reference $MAPbI_3$ film.

We compared the effect of Eu^{3+} by studying other ions, including redox-inert Y^{3+} and strong

oxidizing Fe^{3+}, by preparing film samples incorporated with 1% metal ions (M/Pb, molar ratio) and performed high-resolution X-ray photoelectron spectroscopy (XPS) analysis to elucidate the potential effects on both Pb^0 and I^0 defects. As shown in Fig. 2A**,** the binding energy at 142.8 eV and 137.9 eV were assigned to $4f_{5/2}$, $4f_{7/2}$ of divalent Pb^{2+}, respectively, and the two shoulder peaks at 141.3 eV and 136.4 eV around lower binding energy were associated with metallic Pb^0. We calculated the intensity ratio of $Pb^0/(Pb^0+Pb^{2+})$ for three metal doped samples and the reference to observe a notable tendency (Fig. 2, A and D, and table S1). The Pb^0 intensity ratio in reference reached 5.4%, which is comparable to that of Y^{3+} based film. This ratio in the perovskite film with oxidative Eu^{3+} and Fe^{3+} additives was reduced to nearly 1.0%, indicating that metallic Pb^0 was successfully oxidized.

With respect to I^0 species, it was difficult to obtain $I^0/(I^0+ I^-)$ ratio by peak fitting accurately, because I^0 was volatile during the annealing process of perovskite film preparation. Thus, we examined the ratio of I/Pb and binding energy (BE) shift to monitor the iodine evolution indirectly. As shown in Fig. 2, B and E, and table S1, we observed the similar I/Pb ratio in the reference and the Y^{3+} based sample, but much lower ratio in the Fe^{3+} sample. Incorporation of Fe^{3+} likely generated I^0 species that were released. Interestingly, a higher I/Pb ratio was observed in the Eu^{3+} sample compared to the reference, possibly indicating less volatile I^0 species produced in the corresponding film. Furthermore, the BE of I $3d_{3/2}$ further confirmed the argument, wherein it shifted toward higher value of 0.3 eV in Fe^{3+} sample but lower 0.2 eV in Eu^{3+} sample as compared to the reference. Given the lower BE of I^- was well preserved in the Eu^{3+} sample. In addition, Eu^{2+} was 36% of the total europium content, which further confirmed the Eu^{3+}/Eu^{2+} ion pair working as redox shuttle (Fig.

2C).

According to charge conservation rule, the amount of I^0 should be twice as that of Pb^0 involved in the entire redox reaction. Iodine species (HI and I_2) are all volatile, which follows the 1:2 molar ratio (*33*). We checked the total change of iodine (ΔI) and lead (ΔPb^0) in the film upon the addition of $Eu(acac)_3$, wherein $\Delta I/\Delta Pb^0$ was calculated to be 3.5 (see Table S1 and supplementary text). The change of iodine (ΔI) was three times of the change of lead (ΔPb^0) during degradation process, indicating the I^0 species preserved was twice that of Pb^0 species that was consumed upon redox shuttle addition. In the context of redox reaction, the standard electrode potential (E^θ) is often used as a reference point to rationally predict the occurrence of the reaction. According to E^θ of each half reaction involved (table S2, which may deviate in solid materials), Fe^{3+} is too oxidative and oxidizes Pb^0 and I^- simultaneously. On the contrary, Eu^{3+} exhibited the suitable E^θ to selectively oxidize Pb^0 without I^- oxidation, while the reduction product of Eu^{2+} reduced I^0 to I^- at same time. Thus, the constant elimination of Pb^0, I^0 defects still preserved the Eu^{3+}/Eu^{2+} ion pair.

We examined the effectiveness of Eu^{3+}/Eu^{2+} redox shuttle in the film. Metallic Pb^0 is the major accumulated defect in aged perovskite films because of nonvolatility (*33*). The content of Pb^0 is a measure of the extent of decomposition in the perovskite film. When the sample was subjected to 1 sun illumination or 85 °C aging condition for more than 1000 hours, the $Pb^0/(Pb^0+Pb^{2+})$ ratio in films with redox shuttle were 2.5% or 2.7%, compared to 7.4% or 11.3% in reference film, respectively, as shown in fig. S1 and table S3. The redox shuttle can preserve the element ratio in the aged film. Meanwhile, the corresponding I/Pb ratio in Eu^{3+} based film was 2.68 or 2.57 as compared to that of reference 2.30 or 2.13, indicating the perovskite film was well preserved.

We also examined the crystallographic and optoelectronic properties perovskite films with the redox shuttle. According to XRD results, the phase structure was retained in the perovskite films with improved crystallinity upon Eu^{3+} addition (figs. S2 to S4). No residual acetylacetonate anion was detected by XPS and Fourier transform infrared spectroscopy (FTIR) measurement (fig. S5 and S6). Interestingly, the Eu^{3+}/Eu^{2+} ions were concentrated near the film surface, wherein detected Eu/Pb ratio was much higher than the precursor ratio (table S1). When the $Eu(acac)_3$ was introduced from 0.15% to 4.8%, we observed neither extra diffraction peaks nor an obvious shift of diffraction peaks in the XRD patterns (Figs. S2 to S4), which indicates that Eu^{3+}/Eu^{2+} ions may not necessarily accommodate in the crystal lattice.

Given the similar radius of Eu^{2+} (117 pm (*46*)) and Pb^{2+} (119 pm), however, we cannot confidently rule out the possibility that Eu^{2+} replaces Pb^{2+} at B site, wherein direct evidence is expected. In addition, europium-iodine based organic−inorganic perovskite (47) and lanthanide ions doped $CsPbX_3$ perovskite nanocrystals were found in previous reports (48). The morphology and grain size of the perovskite film with the tiny amount redox shuttle remained similar to the reference (Fig. 3A, fig. S7). Also, we did not observe obvious orientation variation by synchrotron grazing-incidence wide-angle X-ray scattering (GIWAXS) analysis **(**Fig. 3B, fig. S8**)**.

In addition, the optical band gap of the perovskite film upon Eu^{3+} addition was calculated to be 1.55 eV, similar to that of reference (fig. S9). The photoluminescence (PL) intensity (fig. S10) and carrier lifetime (Fig. 3C) increased in the perovskite film with the incorporation of Eu^{3+}, indicating the decrease of nonradiative recombination centers from defects elimination. The improvement of the morphology and grain size could also lead to the increased PL lifetime, so the defects reduction

should be further confirmed by other methods. We used the space charge limited current (SCLC) measurement to quantify a defect density $N_{defects}$, of 5.1×10^{15} and 1.5×10^{16} cm^{-3} for Eu^{3+} incorporated samples and the reference, respectively (Fig. 3D).

We studied the influence of Eu^{3+}/Eu^{2+} ion pair on the formation energies of redox reaction, lattice stability and energy band structure by density-functional theory (DFT) calculations. To construct the model, a small fraction of metal ions (Eu^{3+}) was intercalated into two adjacent lattices (Fig. 3E), given the observation that Eu concentrated at grain boundaries. The formation energies for defects elimination (eqn(1) and eqn(2)) were calculated (Fig. 3F). For both reference and Eu^{3+} incorporated systems, the Pb^0 elimination related half reactions required a substantially high potential energy as the main barrier, while the I^0 elimination half reactions were comparably favorable. However, after introducing europium species at the interface, the barrier in Pb^0 elimination half reactions was greatly decreased but the barrier for I^0 elimination half reactions decreased only slightly. With the assistance of europium species at interface, the overall redox potential energy has been much lowered, representing an energetical stabilization trend for the charge-transfer reaction (Fig. 3F).

We also compared the thermodynamic properties for reference and Eu incorporated systems. Fig. 3G shows that the $CH_3NH_3PbI_3$ with Eu incorporation had a steeper slope in change of free energy ΔG than that of reference, meaning that Eu-incorporated $CH_3NH_3PbI_3$ shows an energetically favorable physicochemical trend than pure $CH_3NH_3PbI_3$. Additionally, it reveals Eu incorporation in $CH_3NH_3PbI_3$ materials did not bring in obvious electronic disorders as extra traps (fig. S11).

We incorporated the perovskite absorber equipped with the redox shuttle in two device configurations. One is based on ITO/TiO_2/perovskite/spiro-OMeTAD/Au, wherein spiro-OMeTAD

refers to 2, 2', 7, 7'-tetrakis-(N,N-di-p-methoxyphenylamine)-9,9'-spirobifluorene, with $MAPbI_3(Cl)$. The other is based on ITO/SnO_2/perovskite/spiro-OMeTAD (modified)/Au for higher PCE and stability, with $(FA,MA,Cs)Pb(I,Br)_3(Cl)$, where FA is formamidinium. Both perovskites were deposited via a traditional two-step method, during which $Eu(acac)_3$ or other additives were added in PbI_2/DMF precursor solution. The two devices showed similar trends (Fig. 4A and fig. S12). The Eu^{3+} based devices exhibited the best PCE, while the Fe^{3+} based ones suffered from the dramatically decreased PCE (fig. S12 and Fig. 4A). The average PCE increased from 18.5% to 20.7% in the mixed perovskite upon Eu^{3+} addition (Fig. 4A), which is attributed to the effective defects elimination. We attributed the decreased PCE in Fe^{3+} based devices to the additional I^0 defects introduced by oxidation.

One of the optimized devices achieved the PCE of 21.52% (reverse 21.89%, forward 21.15%, Fig. 4B) with negligible hysteresis (certified reverse 20.73%, forward 20.30%, average 20.52%, certificate attached in fig. S13). The measured stable output at maximum point (0.97 V) was 20.9%. Integrating the overlap of the incident-photon-to-current-efficiency (IPCE) spectra of Eu^{3+} incorporated PSCs under the AM 1.5G solar photon flux generated the current density of 23.2 $mA \cdot cm^{-2}$ (fig. S14). The stabilized J-V performance of PSCs was evaluated of follows (*49*): parameters are measured under a 13 points IV sweep configuration wherein the bias voltage (current for open circuit voltage V_{OC} determination) is held constant until the measured current (voltage for V_{OC}) was determined to be unchanging at the 0.05% level. The original, stabilized and after stabilized efficiency of Eu^{3+} based PSCs tested by third-party certification institution were similar, which indicates the stable characteristics of the devices (fig. S15).

The shelf lifetime of the corresponding device was investigated, wherein the PCE evolution was descripted for solar cells stored in inert environment (Fig. 4C). With Eu^{3+}/Eu^{2+} redox shuttle incorporated, the device maintained 90% of its original PCE even after 8000 hours storage due to improved long-term V_{OC}, short-circuit current density (J_{SC}) and fill factor (FF) stability (fig. S16). Although the stability of Y^{3+} based PSCs was comparable to the reference, Fe^{3+} based perovskite solar cells showed severely deteriorated stability, which lost the photoelectric conversion capability completely after merely 2000 hours storage.

To estimate the stability of Eu^{3+} incorporated perovskite solar cells under operational conditions, devices were subjected to either continuous 1 sun illumination or 85 °C aging condition, respectively (Fig. 4D) , in which the top charge-transfer materials and electrode were deposited after aging test. Improved long-term V_{OC} and FF stability (fig. S17) allowed the device, after 1000 hours, to retain 93% of its original PCE continuous 1 sun illumination or 91% after heating to 85 °C. Several previous studies showed that small molecule spiro-OMeTAD would crystallize under thermal stress and create pathways that allow for an interaction of the perovskite and the metal electrode (*50, 51*). By modifying the hole-transport materials (spiro-OMeTAD), the full devices based on Eu^{3+}/Eu^{2+} ion pair maintained 92% and 89% of original PCE due to obvious long-term V_{OC} and FF stability improvement (fig. S18) under the same light or thermal stress for 1500 hours, respectively (Fig. 4E). Furthermore, the Eu^{3+} based whole device could maintain 91% of its original stable PCE tracked at maximum power point (MPP) for 500 hours (Fig. 4F).

REFERENCES AND NOTES

1. A. Kojima *et al.,* Organometal halide perovskites as visible-light sensitizers for photovoltaic cells. *J. Am. Chem. Soc.* **131**, 6050-6051 (2009). doi: 10.1021/ja809598r

2. M. M. Lee *et al.*, Efficient hybrid solar cells based on meso-superstructured organometal halide perovskites. *Science* **338**, 643-647 (2012). doi: 10.1126/science.1228604

3. H. Zhou *et al*., Interface engineering of highly efficient perovskite solar cells. *Science* **345**, 542-546 (2014). doi: 10.1126/science.1254050

4. J.-H. Im *et al.*, Growth of $CH_3NH_3PbI_3$ cuboids with controlled size for high-efficiency perovskite solar cells. *Nat. Nanotechnol*. **9**, 927-932 (2014). doi: 10.1038/nnano.2014.181

5. M. Yang *et al.*, Square-centimeter solution-processed planar $CH_3NH_3PbI_3$ perovskite solar cells with efficiency exceeding 15%. *Adv. Mater.* **27**, 6363-6370 (2015). doi:10.1002/adma.201502586

6. O. Malinkiewicz *et al.*, Perovskite solar cells employing organic charge-transport layers. *Nat. Photonics* **8**, 128-132 (2014). doi: 10.1038/nphoton.2013.341

7. W. S. Yang *et al.*, High-performance photovoltaic perovskite layers fabricated through intramolecular exchange. *Science* **348**, 1234-1237 (2015). doi: 10.1126/science.aaa9272

8. W. S. Yang *et al.*, Iodide management in formamidinium-lead-halide–based perovskite layers for efficient solar cells. *Science* **356**, 1376-1379 (2017). doi: 10.1126/science.aan2301

9. National Renewable Energy Laboratory (NREL) Efficiency chart. https://www.nrel.gov/pv/assets/images/efficiency-chart-20180716.jpg (2018).

10. N. H. Tiep *et al*, Recent advances in improving the stability of perovskite solar cells. *Adv. Energy Mater.* **6**, 1501420 (2016). doi: 10.1002/aenm.201501420

11. Y. Rong *et al*, Beyond efficiency: the challenge of stability in mesoscopic perovskite solar cells. *Adv. Energy Mater.* **5**, 1501066 (2015). doi: 10.1002/aenm.201501066

12. T. A. Berhe *et al.*, Organometal halide perovskite solar cells: degradation and stability. *Energy Environ. Sci.* **9**, 323-356 (2016). doi: 10.1039/c5ee02733k

13. G. Grancini *et al.*, One-Year stable perovskite solar cells by 2D/3D interface engineering. *Nat Commun.* **8**, 15684 (2017). doi: 10.1038/ncomms15684

14. J. P. Correa-Baena *et al.*, Promises and challenges of perovskite solar cells. *Science* **358**, 739-744 (2017). doi: 10.1126/science.aam6323

15. D. C. Jordan *et al*, Photovoltaic Degradation Rates-an Analytical Review. *Prog. Photovolt: Res. Appl.* **21**, 12-29 (2013). doi: 10.1002/pip.1182

16. Q. Cao *et al.*, Defects in Cu(In, Ga)Se_2 chalcopyrite semiconductors: a comparative study of material properties, defect states, and photovoltaic performance. *Adv. Energy Mater.* **1**, 845-853 (2011). doi: 10.1002/aenm.201100344

17. F. De Angelis *et al.*, Trends in Perovskite Solar Cells and Optoelectronics: Status of Research and Applications from the PSCO Conference. *ACS Energy Lett.* **2**, 857-861 (2017). doi: 10.1021/acsenergylett.7b00217

18. J. M. Frost *et al.*, Atomistic origins of high-performance in hybrid halide perovskite solar cells. *Nano Lett.* **14**, 2584-2590 (2014). doi: 10.1021/nl500390f

19. Z. Yu *et al.*, Recent Progress on Hole-Transporting Materials for Emerging Organometal Halide Perovskite Solar Cells. *Adv. Energy Mater.* **5**, 1500213 (2015). doi: 10.1002/aenm.201500213

20. W. Li *et al.*, Effect of cesium chloride modification on the film morphology and UV-induced stability of planar perovskite solar cells. *J. Mater. Chem. A*, **4**, 11688–11695 (2016). doi: 10.1039/c5ta09165a

21. W. Li *et al.*, Enhanced UV-light stability of planar heterojunction perovskite solar cells with caesium bromide interface modification. *Energy Environ. Sci.* **9**, 490-498 (2016). doi: 10.1039/c5ee03522h

22. M. Saliba *et al.*, Incorporation of rubidium cations into perovskite solar cells improves photovoltaic performance. *Science* **354**, 206-209 (2016). doi: 10.1126/science.aah5557

23. M. Hösel *et al.*, Comparison of UV-Curing, Hotmelt, and Pressure Sensitive Adhesive as Roll-to-Roll Encapsulation Methods for Polymer Solar Cells. *Adv. Eng. Mater.* **15**, 1068-1075 (2013). doi: 10.1002/adem.201300172

24. Y. Han *et al.*, Degradation observations of encapsulated planar $CH_3NH_3PbI_3$ perovskite solar cells at high temperatures and humidity. *J. Mater. Chem. A* **3**, 8139-8147 (2015). doi: 10.1039/c5ta00358j

25. Y. Li *et al.*, Multifunctional fullerene derivative for interface engineering in perovskite solar cells. *J. Am. Chem. Soc.* **137**, 15540-15547 (2015). doi: 10.1021/jacs.5b10614

26. H. Azimi *et al.*, A Universal Interface Layer Based on an Amine-Functionalized Fullerene Derivative with Dual Functionality for Efficient Solution Processed Organic and Perovskite Solar Cells. *Adv. Energy Mater.* **5**, 1401692 (2015). doi: 10.1002/aenm.201401692

27. J. Cao *et al.*, Thiols as interfacial modifiers to enhance the performance and stability of perovskite solar cells. *Nanoscale* **7**, 9443-9447 (2015). doi: 10.1039/c5nr01820j

28. X. Li *et al.*, Improved performance and stability of perovskite solar cells by crystal crosslinking with alkylphosphonic acid ω-ammonium chlorides. *Nat. Chem.* **7**, 703-711 (2015). doi: 10.1038/nchem.2324

29. W. Peng *et al.*, Engineering of $CH_3NH_3PbI_3$ perovskite crystals by alloying large organic cations for enhanced thermal stability and transport properties. *Angew. Chem. Int. Ed.* **55**, 10686-10690 (2016). doi: 10.1002/anie.201604880

30. R. K. Gunasekaran *et al.*, Revealing the Sel-Degradation Mechanisms in Methylammonium Lead Iodide Perovskites Stored in Dark and Vacuum. *ChemPhysChem* **19**, 1–8 (2018). doi: 10.1002/cphc.201800002

31. S. Wang *et al.*, Accelerated degradation of methylammonium lead iodide perovskites induced by exposure to iodine vapour. *Nat. Energy* **2**, 16195 (2017). doi :10.1038/nenergy.2016.195

32. S. R. Raga *et al.*, Influence of air annealing on high efficiency planar structure perovskite solar cells. *Chem. Mater.* **27**, 1597-1603 (2015). doi: 10.1021/cm5041997

33.Y. Li *et al.*, Light-induced degradation of $CH_3NH_3PbI_3$ hybrid perovskite thin film. *J. Phys. Chem. C* **121**, 3904-3910 (2017). doi: 10.1021/acs.jpcc.6b11853

34. B. Philippe *et al.*, Valence Level Character in a Mixed Perovskite Material and Determination of the Valence Band Maximum from Photoelectron Spectroscopy: Variation with Photon Energy. *J. Phys. Chem. C* **121**, 26655-26666 (2017). doi: 10.1021/acs.jpcc.7b08948

35. H. Cho *et al.*, Overcoming the electroluminescence efficiency limitations of perovskite light-emitting diodes. *Science* **350**, 1222-1225 (2015). doi: 10.1126/science.aad1818

36. V. Adinolfi *et al.*, The In-Gap Electronic State Spectrum of Methylammonium Lead Iodide Single-Crystal Perovskites. *Adv. Mater.* **28**, 3406-3410 (2016). doi: 10.1002/adma.201505162

37. G. W. Hwang *et al.*, Identifying and Eliminating Emissive Sub-bandgap States in Thin Films of PbS Nanocrystals. *Adv. Mater.* **27**, 4481-4486 (2015). doi: 10.1002/adma.201501156

38. A. Friedenberg *et al.*, Photolysis and conductivity measurements at PbI_2 surfaces. *Surface Sci.* **115**, 606-622 (1982). doi: 10.1016/0039-6028(82)90391-0

39. X. Tang *et al.*, Photoinduced degradation of methylammonium lead triiodide perovskite semiconductors. *J. Mater. Chem. A* **4**, 15896-15903 (2016). doi: 10.1039/c6ta06497c

40. R. Purbia *et al.*, An Au/AgBr–Ag heterostructure plasmonic photocatalyst with enhanced catalytic activity under visible light. *Dalton T.* **46**, 890-898 (2017). doi: 10.1039/c6dt03723b

41. H. Xie *et al.*, Effects of Precursor Ratios and Annealing on Electronic Structure and Surface Composition of $CH_3NH_3PbI_3$Perovskite Films. *J. Phys. Chem. C* **120**, 215-220 (2016). doi: 10.1021/acs.jpcc.5b07728

42. C. Qin *et al.*, Multifunctional benzoquinone additive for efficient and stable planar perovskite solar cells. *Adv. Mater.* **29**, 1603808 (2017). doi: 10.1002/adma.201603808

43. W. Zhang *et al.*, Enhanced optoelectronic quality of perovskite thin films with hypophosphorous acid for planar heterojunction solar cells. *Nat. Commun.* **6**, 10030 (2015). doi: 10.1038/ncomms10030

44. Z. Liu *et al.*, Chemical Reduction of Intrinsic Defects in Thicker Heterojunction Planar Perovskite Solar Cells. *Adv. Mater.* **29**, 1606774 (2017). doi: 10.1002/adma.201606774

45. D. R. Lide, *Handbook of Chemistry and Physics*, 84th ed., **5,** 5-60 (2003).

46. P. Jakubcova *et al.*, Structure and Properties of Mixed-valence Compound $Eu_5Zr_3S_{12}$. Z. *Anorg, Allg. Chem.* **635**, 759-763 (2009). doi: 10.1002/zaac.200900075

47. D. B. Mitzi *et al.,* Preparation and properties of $(C_4H_9NH_3)_2EuI_4$: A luminescent organic−inorganic perovskite with a divalent rare-earth metal halide framework. *Chem. Mater.* **9**, 2990-2995 (1997). doi: 10.1021/cm970352d

48. G. Pan *et al.*, Doping lanthanide into perovskite nanocrystals: highly improved and expanded optical properties. *Nano Lett.* **17**, 8005-8011 (2017). doi: 7 10.1021/acs.nanolett.7b04575

49. ASTM E948-16, Standard Test Method for Electrical Performance of Photovoltaic Cells Using Reference Cells Under Simulated Sunlight. *ASTM International* (2016). doi: 10.1520/E0948-16

50. T. Malinauskas *et al.*, Enhancing thermal stability and lifetime of solid-state dye-sensitized solar cells via molecular engineering of the hole-transporting material spiro-OMeTAD. *ACS Appl. Mater. Interfaces* **7**, 11107-11116 (2015). doi: 10.1021/am5090385

51. K. Domanski *et al.*, Not all that glitters is gold: Metal-migration-induced degradation in perovskite solar cells. *ACS Nano* **10**, 6306-6314 (2016). doi: 10.1021/acsnano.6b02613

52. L. Wang *et al.*, A-Site Cation Effect on Growth Thermodynamics and Photoconductive Properties in Ultrapure Lead Iodine Perovskite Monocrystalline Wires. *ACS Appl. Mater. Interfaces* **9**, 25985−25994 (2017). doi: 10.1021/acsami.7b05875

53. S. J. Clark *et al.*, First principles methods using CASTEP. *Z. Kristallogr.* **220**, 567-570 (2005). doi: 10.1524/zkri.220.5.567.65075

54. J. P. Perdew *et al.*, Atoms, molecules, solids, and surfaces: Applications of the generalized gradient approximation for exchange and correlation. *Phys. Rev. B* **46**, 6671-6687 (1992). doi: 10.1103/PhysRevB.46.6671

55. J. P. Perdew *et al.*, Generalized Gradient Approximation Made Simple. *Phys. Rev. Lett.* **77**, 3865-3868 (1996). doi: 10.1103/PhysRevLett.78.1396

56. A. M. Rappe *et al.*, Erratum: Optimized pseudopotentials. *Phys. Rev. B* **44**, 13175-13176 (1991). doi: 10.1103/PhysRevB.44.13175.3

57. S. G. Bratsch, Standard electrode potentials and temperature coefficients in water at 298.15 K. *J. Phys. Chem. Ref. Data* **18**, 1-21 (1989). doi: 10.1063/1.555839

ACKNOWLEDGMENTS

The manuscript was improved by the insightful reviews by the anonymous reviewers. The authors appreciate the insightful data analysis and valuable discussion with Prof. Yang Yang (University of California, Los Angeles), Prof. Yujing Li (Beijing Institute of Technology), Prof. Haipeng Xie (Central South University), Prof. Qinye Bao (East China Normal University) and Dr. Jiawen Xiao (Beijing Institute of Technology). The authors sincerely appreciate the third certification institutions, National Institute of Metrology (China) and Newport Technology and Application Center PV Lab (USA), for authentication tests. The authors thank beamline BL14B1 (Shanghai Synchrotron Radiation Facility, SSRF) for providing the beam time and help during the experiments. The authors

appreciate Enli technology co. Ltd. for their help regarding PV efficiency and EQE measurement. **Funding:** This work was supported by National Natural Science Foundation of China (Nos. 51722201, 51672008, 91733301, 21425101, 21331001, 21621061), MOST of China (2014CB643800), National Key Research and Development Program of China Grant (No. 2017YFA0206701, and 2017YFA0205101) Beijing Natural Science Foundation 4182026, Young Talent Thousand Program. **Author contributions:** L.W. and H.Z. conceived the idea and designed the project. H.Z., C.H.Y. and L.D.S. directed and supervised the research. L.W. fabricated and characterized devices. Y.H., Y.C., L.L., Z.X., N.L. also contributed to devices fabrication. L.W. performed the SEM, PL, UPS, UV-Vis, XPS, XRD measurements. GIWAX was performed and analyzed by G.Z., supported by BL14B1 beamline of SSRF. B. D. and Z.L. performed EPR. M.S. and B.H. carried out DFT calculation. L.W. drafted the manuscript; Q.C. and H.Z. revised and finalized the manuscript. **Competing interests**: The authors have no competing interests. **Data and materials availability**: All data are available in the main text or the supplementary materials.

SUPPLEMENTARY MATERIALS

www.sciencemag.org

Materials and Methods

Supplementary Text

Figs. S1 to S18

Tables S1 to S3

References 52 to 57

25 June 2018; resubmitted 25 September 2018

Accepted XX XXXX 2018.

Published online XX XXXX 2018

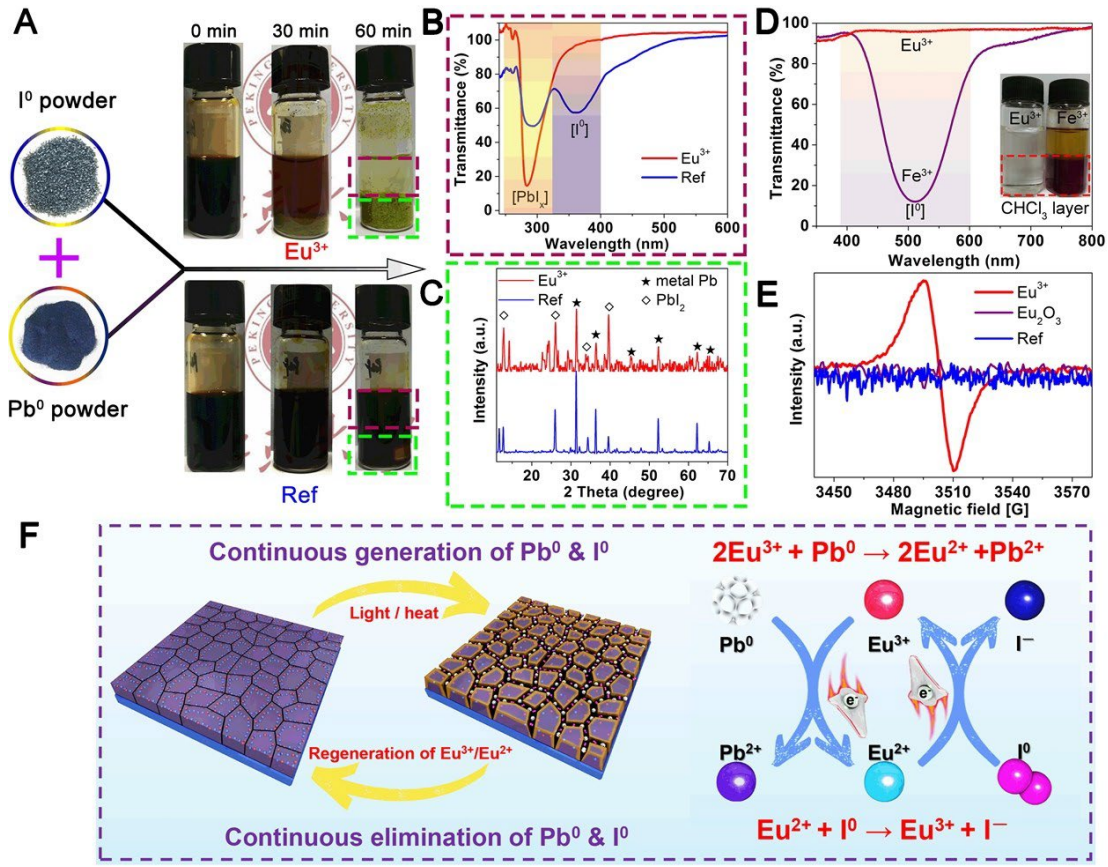

Fig. 1. Eu^{3+}/Eu^{2+} ion pair promotes the conversion of Pb^0 and I^0 to Pb^{2+} and I^- in solution and perovskite film. (**A**) I^0 and Pb^0 powder dispersed in mixed DMF/IPA solvent (volume ratio 1:10) with or without Eu^{3+} (europium acetylacetonate ($Eu(acac)_3$)), and the solution was stirred at 100 °C. (**B**) The ultraviolet-visible (UV-Vis) absorption spectra of upper solution from two samples (after 60 min) shown in A. (**C**) XRD patterns of the bottom precipitation from two samples (after 60 min) shown in A. (**D**) The representative solution and the absorption spectra of bottom layer in which MAI mixed with Eu^{3+} or Fe^{3+} dissolved in water/$CHCl_3$. (**E**) Electron paramagnetic resonance (EPR) spectra of $MAPbI_3$ with or without Eu^{3+} incorporation, and Eu_2O_3 film, where the value of proportionality factor (g-factor) is 2.0023. (**F**) Proposed mechanism diagram of cyclically elimination of Pb^0 and I^0 defects and regeneration of Eu^{3+}/Eu^{2+} metal ion pair.

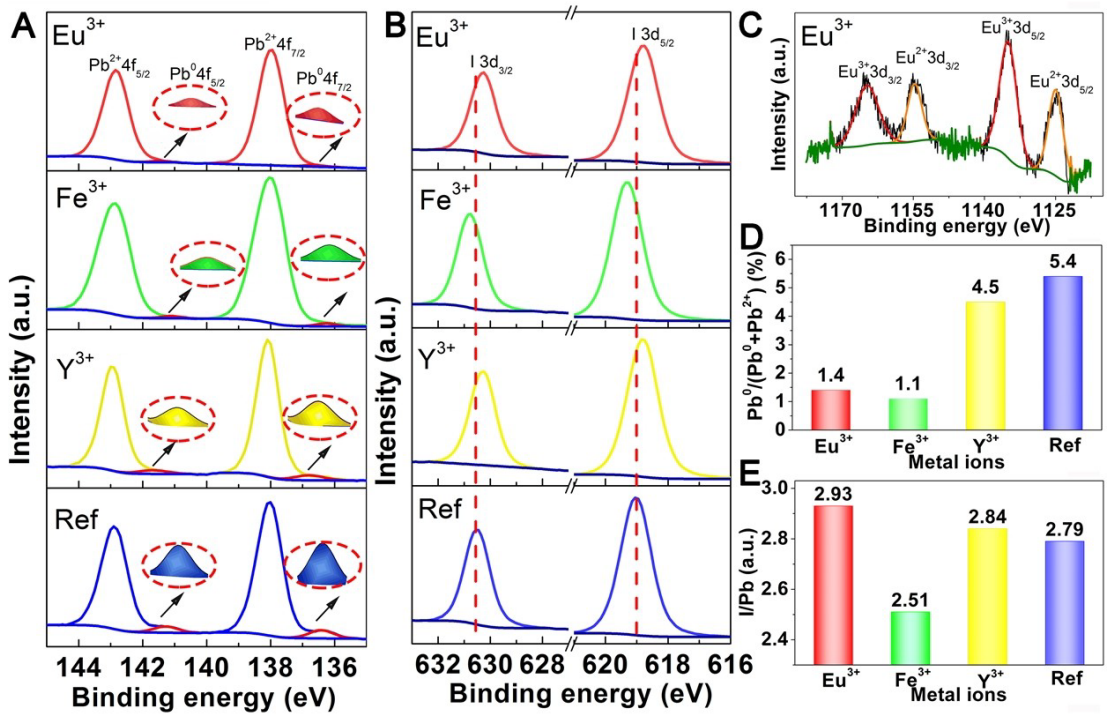

Fig. 2. High-resolution XPS spectra of Pb 4f, I 3d and the Eu 3d of perovskite films with the incorporation of 1% M/Pb different acetylacetonate metal salts ($M(acac)_3$, M = Eu^{3+}, Y^{3+}, Fe^{3+}). (**A**) Pb 4f spectra, the insertions are the enlarged spectra of Pb^0 4f. (**B**) I 3d spectra. (**C**) Eu 3d spectra. (**D**) Fitted results of Pb^0/Pb^0+Pb^{2+} ratio. (**E**) Fitted results of I/Pb ratio.

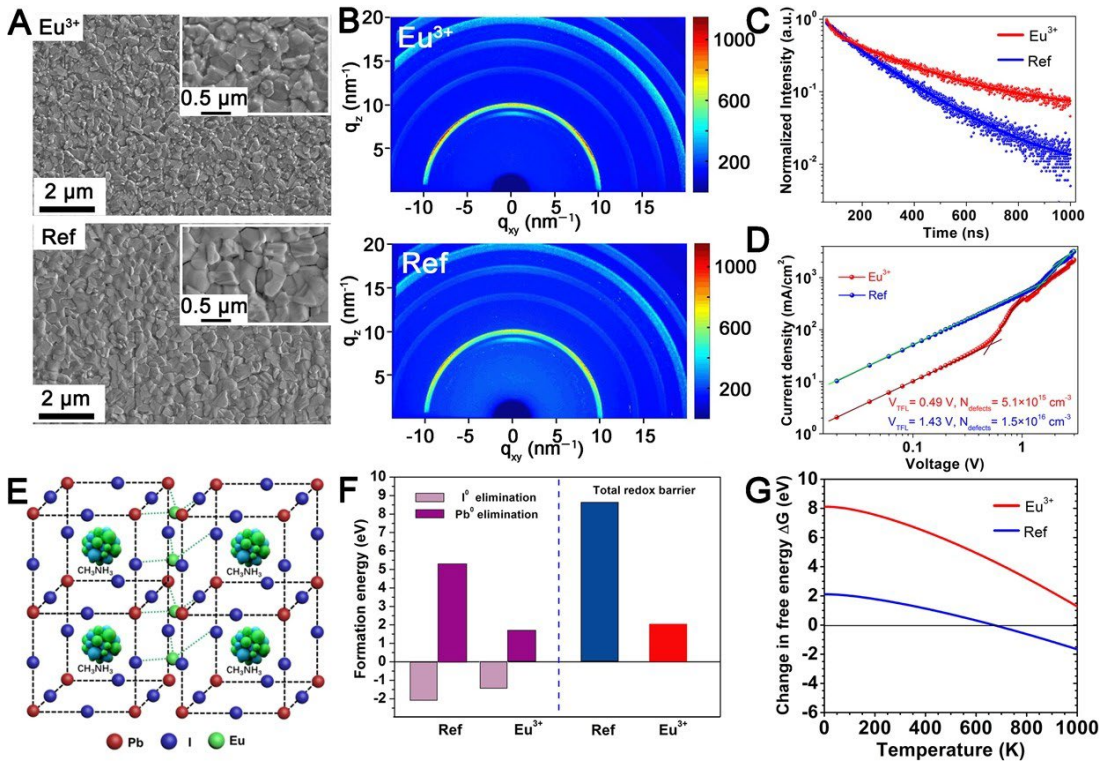

Fig. 3. Influence of morphology, orientation, electronic structure, carrier behaviors of Eu^{3+} ion incorporated perovskite film and results of density-functional theory (DFT) calculations. The characterization of reference and 0.15% Eu^{3+} incorporated perovskite film: (**A**) SEM images; (**B**) GIWAXS data; (**C**) TRPL; (**D**) J-V characteristics of devices (ITO/perovskite/Au), utilized for estimating the SCLC defects concentration ($N_{defects} = 2\varepsilon\varepsilon_0 V_{TFL}/eL^2$, ε and ε_0 are the dielectric constants of perovskite and vacuum permittivity, L is the thickness of the perovskite film, and e is the elementary charge). (**E**) The interface ultra-thin Eu clustering-layer incorporated structural model. (**F**) Left: half-reaction potential barriers; Right: overall redox charge transfer reaction barrier for Eu incorporated at the interface. (**G**) The summary of ΔG between $CH_3NH_3PbI_3$ and $CH_3NH_3PbI_3$ incorporated with Eu in the interface.

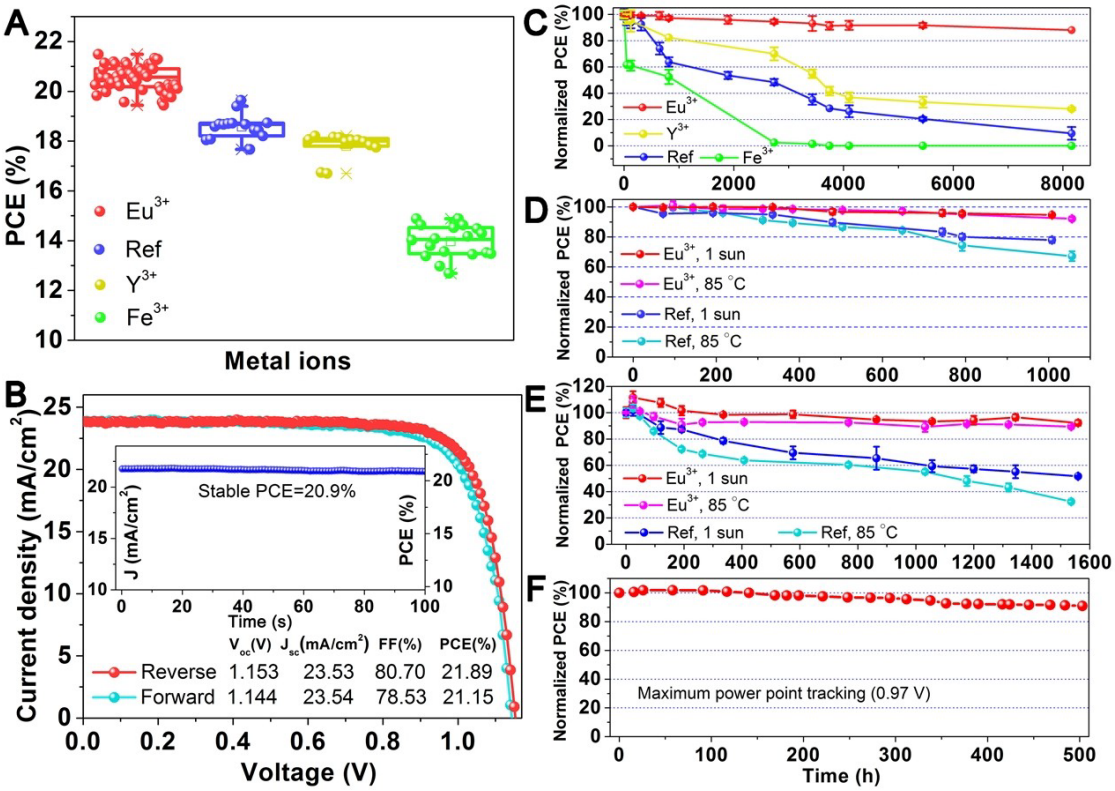

Fig. 4. **Long-term stability and original performance evolution of PSCs.** (**A**) Original performance evolution based on (FA,MA,Cs)Pb(I,Br)$_3$(Cl) perovskite with the incorporation of 0.15% different M(acac)$_3$ (M = Eu^{3+}, Y^{3+}, Fe^{3+}). (**B**) The J-V curve, stable output (measured at 0.97 V) and parameters of 0.15% Eu^{3+} incorporated champion devices. (**C**) Long-term stability of PSCs based on $MAPbI_3$(Cl) perovskite absorber with the incorporation of 0.15% different (M(acac)$_3$ (M = Eu^{3+}, Y^{3+}, Fe^{3+}), stored in inert condition. The PCE evolution of Eu^{3+}/Eu^{2+} based sample and reference devices under 1 sun illumination or 85 °C aging condition: (**D**) half PSCs (original PCE: 0.15% Eu^{3+} incorporated PSCs, 19.21 ± 0.54%; reference PSCs, 18.05 ± 0.38%) and (**E**) full PSCs (original PCE: 0.15% Eu^{3+} incorporated PSCs, 19.17 ± 0.42%; reference PSCs, 17.82 ± 0.30%). Scanning speed is 20 mV/s. (**F**) The MPP tracking of 0.15% Eu^{3+} incorporated device, measured at 0.97 V and 1 sun illumination